Transparent conducting oxide films with p-type characteristics derived from sol-gel dip-coating of LaF$_3$- and CeF$_3$-doped tin oxides

Van-Da Dao[1, *], Quang-Phu Tran[1, *], Van-Hoi Pham[2]

[1]Department of Electrical and Electronic Engineering, Hung Yen University of Technology and Education, Viet Nam

[2]Institute of Materials Science, Vietnam Academy of Science and Technology, 18 Hoang Quoc Viet, Cau Giay, Ha Noi, Viet Nam

[*]Email: tranquangphu@utehy.edu.vn

Abstract. Transparent semiconductor oxide films, typically based on doped indium tin oxide, find widespread use in optoelectronic devices. Since tin oxide films inherently exhibit n-type conductivity, achieving efficient p-type tin oxide film electrodes is a challenging task for applications in p-n based photonic devices. In this investigation, we introduce innovative p-type transparent films whose optical transmittance and electrical resistivity can be adjusted by doping tin oxide films with various rare-earth triflouride compouds such as LaF$_3$ and/or CeF$_3$ using sol-gel dip-coating method. The p-type conductance of the thin films is confirmed through Hall effect and Seebeck coefficient measurements. The obtained results indicate that the LaF$_3$- and CeF$_3$-doped SnO$_2$ films exhibited an average optical transmittance of 84.3 % and 82.0 % in the visible light range, a low electrical resistivity of 8.68×10^{-3} Ωcm and 1.70×10^{-2} Ωcm, and a high figure-of-merit of 6.59×10^{-4} Ω^{-1} and 1.74×10^{-4} Ω^{-1}, respectively, making them highly suitable for applications in optoelectronics.

Keywords: Rare-earth tri-fluoride doped tin oxide films, p-type transparent conducting oxide films, sol-gel dip-coating method, optical and electrical properties.

Classification numbers: 2.1.1, 2.1.3, 2.5.2, 2.10.2.

1. INTRODUCTION

Transparent conducting oxide films (TCOs) are metallic oxides that have been extensively researched and employed in optoelectronic devices [1 - 5] because they simultaneously possess unique properties of electrical conductivity and optical transparency. High quality TCO film should exhibit high electrical conductivity and optical transparency, or high figure-of-merit (FOM) that combines the two factors [6]. The structural formation of optoelectronic devices requires p-type and n-type semiconductor layers, and the performance of these devices depends greatly on the quality of the TCO films. The majority of literature reports focusing on effective

TCO so far predominantly involve n-type variants, characterized by optical transmittance surpassing 80 % and electrical resistivity reaching 10^{-4} Ωcm [4, 7]. Yet, obtaining p-type TCOs of comparable quality to n-type TCOs proves to be a challenging task. Currently, one of the most noteworthy p-type TCOs is AZO:Cu_2O, as reported by Hui *et al.*, displaying an electrical resistivity of 6.94×10^{-3} Ωcm and optical transparency exceeding 90 % [8]. Following the initial publication in 1997 by Kawazoe *et al.* concerning p-type transparent conducting thin films utilizing $CuAlO_2$ through pulsed laser deposition [9], numerous endeavors have been undertaken to produce p-type transparent conducting thin films, employing diverse deposition techniques and a range of materials [8, 10 - 15].

Various methods have been employed for film preparation, including pulsed laser deposition [10-12], hydrothermal synthesis [13], spray pyrolysis technique [14], and/or the sol-gel spin coating method [8, 15]. On the other hand, materials utilized for fabricating transparent electrodes primarily consist of compounds such as binary oxides (NiO, SnO, and Cu-based oxides) [16], ternary oxides ($CuGaO_2$ [10], $CuBO_2$ [11], $CuCrO_2$ [13], $AgGaO_2$ [12], $FeSnO_2$ [14]), or multi-component oxides ($InGaO_3(ZnO)_5$ [17], Cu:ZnCoO [15], AZO:Cu_2O [8], LaCuOS [18], ($La_{1-x}Sr_xO$)CuS [19], NdCuOS:Mg5% [3]). The oxygen layer comprises various materials that enhance the flexibility to modify its electrical and optical properties by adjusting the chemical composition. Notably, layered oxychalcogenide film compounds incorporating rare-earth elements such as ($La_{1-x}Sr_xO$)CuS [19] or NdCuOS:Mg5% [3] exhibit p-type conductivity along with high electrical conductivity and optical transparency. Banerjee *et al.* suggested employing rare earth elements like La^{3+}, Pr^{3+}, Nd^{3+}, Sm^{3+}, etc. in the synthesis of layered oxychalcogenide films, with promising outcomes for numerous optoelectronic applications [20].

In this work, we aim to regulate the electrical and optical characteristics of tin oxides doped with rare-earth trifluorides (RFTO). The RFTO thin films were produced using the sol-gel dip-coating method. The chosen rare-earth trifluorides (RF_3) compounds for doping include lanthanum trifluoride (LaF_3) and cerium trifluoride (CeF_3). The selection of LaF_3 and CeF_3 is based on two primary considerations: 1) the abundance of rare-earth elements, with La and Ce constituting approximately 30 % and 60 %, respectively, of the total rare-earths in the Earth's crust [21]; 2) the stability of these constituents, allowing them to withstand non-vacuum processing methods like sol-gel dip-coating, which is prone to ambient oxidation. Rare-earth trifluorides are recognized for their high stability, with melting points of 1493 °C for LaF_3 and 1460 °C for CeF_3 [22]. The study explores the impact of RF_3 on the conduction type, structure, as well as the electrical and optical properties of the films.

2. MATERIALS AND METHODS

2.1. Chemicals

To prepare the gel solution, a mixture comprising 0.7 M tin chloride penta-hydrate ($SnCl_4 \cdot 5H_2O$, Acros Organics, purity 99.0 %), and 0.7 M monoethanolamine (MEA, [C_2H_7NO], Sigma-Aldrich, purity 99 %) was dissolved in 2-methoxyethanol ([$C_3H_8O_2$], Sigma-Aldrich, purity 99.5 %) as the initial solution. In this process, tin chloride penta-hydrate, monoethanolamine, and 2-methoxyethanol served as the tin source, stabilizer, and solvent, respectively. The initial solution volume was 100 mL. Three identical initial solutions were placed into individual beakers. These three solutions were stirred for 3 hours at 80 °C, resulting in the formation of a yellowish and clear solution. LaF_3 (Acros Organics, purity 99.9 %) and

CeF_3 (Acros Organics, purity 99.9 %), were employed as sources for lanthanum- and cerium-fluorine dopants, respectively. Separate additions of LaF_3 and CeF_3, each at a concentration of 2 mol.%, were introduced into the two beakers containing the initial solution. To facilitate the complete dissolution of LaF_3 and CeF_3 into the first solution, 5 mol/L nitric acid (HNO_3, Sigma-Aldrich, 71 %) was added. The two resulting solutions were continuously stirred at 80 °C for 3 hours. Following this, the solutions (which comprised a beaker of initial solution) were allowed to age at ambient temperature for 6 days, leading to the creation of a transparent and yellowish solution.

2.2. Synthesis of material and preparation of thin films

Un-doped and RF_3-doped SnO_2 thin films were applied to the Corning EAGLE XG™ glass substrate using the dip-coating method. The glass substrate with the size of 35 mm × 35 mm × 0.5 mm underwent a thorough cleaning process, involving washing with detergent, rinsing with distilled water, ultrasonication in an ethanol-acetone mixture, and subsequent rinsing with distilled water. The samples were produced using the sol-gel dip-coating technique. We fabricated and utilized a dip-coater equipped with a stepper motor, which integrated a ball screw with a microcontroller. The substrate was immersed in the prepared solution for a duration of 1 minute, then vertically withdrawn at a constant speed of 3.5 cm/min. Subsequently, the samples underwent drying at 130 °C for 10 minutes to eliminate the solvent and residual organic substances. Afterward, they were allowed to cool naturally to room temperature. This process was iterated six times to increase the thickness of the film. The dried films were subjected to a post-annealing process in air at 475 °C for a duration of 1 hour.

2.3. Characterization

We employed a Microfigure Measuring Instrument Surfcorder - ET300 for measuring the film thickness. X-ray diffraction analysis (XRD) was conducted to examine the structure of the films using a Bruker-D8SS diffractometer. A field-emission-scanning-electron-microscope (FESEM, HITACHI/S–4800) was used to observe surface morphology of the films. A spectrophotometer (Shimadzu UV 1601) was utilized for measuring optical parameters. Electrical resistivity and Hall effect measurements were conducted using equipment provided by Jiehan Technology Corporation, Taiwan. The electrical resistivity was determined using a four-point probe method, while Hall effect measurements were performed with a Hall probe on a printed circuit board under a magnetic field of 0.53 T, following the van der Pauw configuration. Seebeck coefficient measurements were carried out to verify the conduction type of the films. For these measurements, pairs of microheaters and thermocouples were used to control and measure the temperature difference (ΔT; 300 - 345 K) between two specific points on the sample. Concurrently, the Seebeck voltages (ΔV) between these two points were detected through a pair of thin Cu wires connected to a Keithley 2700 data acquisition system. Subsequently, the Seebeck coefficient ($\Delta V/\Delta T$) could be determined.

3. RESULTS AND DISCUSSION

3.1. Structural analysis
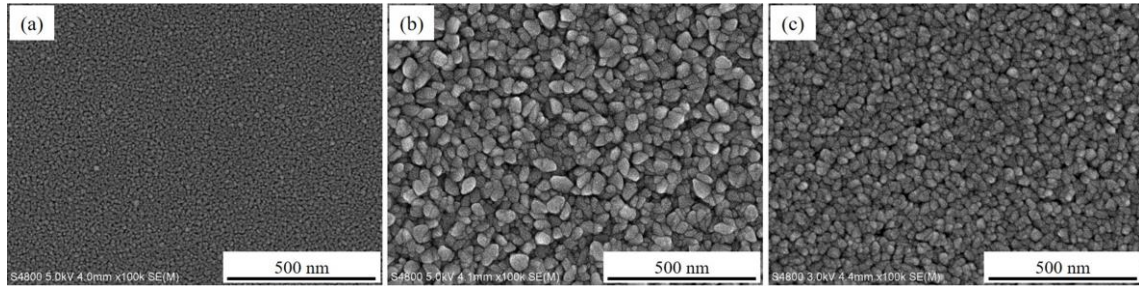
Figure 1. Surface morphologies observed through SEM of tin oxide films doped with rare-earth fluoride: (a) un-doped SnO_2; (b) 2 mol.% LaF_3-doped SnO_2; and (c) 2 mol.% CeF_3-doped SnO_2.
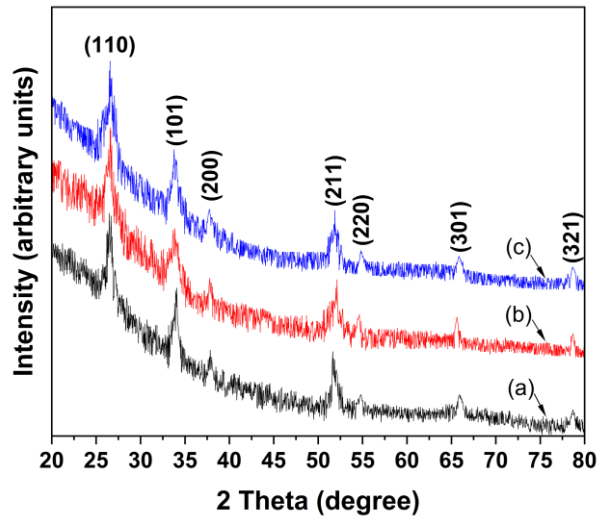
Figure 2. X-ray diffraction patterns of tin oxide thin films doped with rare-earth fluoride: (a) un-doped SnO_2; (b) 2 mol.% LaF_3-doped SnO_2; and (c) 2 mol.% CeF_3-doped SnO_2.

Surface morphologies of both un-doped and RF_3-doped SnO_2 thin films were presented in Figure 1. The films exhibit a composition of compact nanometer-sized granules. The surface morphologies across all films appear uniform and devoid of any discernible cracks. Figure 2 illustrates the XRD patterns of SnO_2 films after post-annealing. The diffraction patterns confirm the presence of a tetragonal rutile structure in all films, with dominant peaks at (110), (101), (200), (211), (220), (301), and (321) (JCPDS #41-1445), indicating a preferred orientation along the (110) plane and a random orientation resembling to powder pattern. The LaF_3-doped SnO_2 (LFTO) film exhibits the highest peak intensity, slightly decreasing in the CeF_3-doped SnO_2 (CFTO) film. This suggests that the crystalline quality of RFTO films diminishes with the atomic number of the rare-earth elements doped in the SnO_2 films. The Full-Width-at-Half-Maximum (FWHM) derived from the (110) peak of the films is presented in Table 1, showing a slight reduction in FWHM for RFTO films compared to the un-doped SnO_2 film, with the LFTO film having the smallest value. The grain size of RF_3-doped SnO_2 films was determined by applying Scherrer's formula [4] to the FWHM of the (110) peaks. The average grain size of the un-doped SnO_2 film is 17.7 nm, significantly increasing to 40.7 nm with 2 mol.% LaF_3 doping. Meanwhile, the addition of 2 mol.% CeF_3 in CFTO films results in a slight increase in grain size,

127

reaching 22.8 nm. The enhanced grain size observed in 2 mol.% LaF_3-doped SnO_2 and 2 mol.% CeF_3-doped SnO_2 films compared to un-doped SnO_2 films may be attributed to variations in lattice energy resulting from the doping of RF_3 into the SnO_2 lattice, consequently influencing the rate of grain growth. The granular structure, grain size, and shape of RF_3-doped SnO_2 films, as compared to the un-doped SnO_2 film in Figure 1, show variations that align with the XRD findings presented in Figure 2.

Table 1. Full-width-at-half-maximum, grain size, thickness, optical transmittance, and optical band gap of un-doped and 2 mol.% RF_3-doped SnO_2 thin films.

Film	FWHM (degree)	Grain size (nm)	Thickness (nm)	Transmittance (%)	Optical band gap (eV)
SnO_2	0.575	17.7	228	87.1	3.95
LFTO	0.258	40.7	287	84.3	3.81
CFTO	0.426	22.8	246	82.0	3.74

The thickness of SnO_2 films after the post-annealing process was determined through step height measurement and is provided in Table 1. The un-doped SnO_2 film measures 228 nm in thickness. In comparison, with the same dipping times, the thickness of LFTO and CFTO shows a slight increase, measuring 287 nm and 246 nm, respectively.

3.2. Optical properties
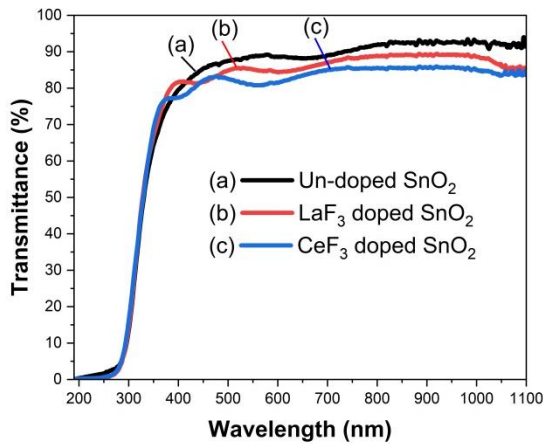
Figure 3. Transmittance spectra of post-annealed rare-earth-fluoride-doped tin oxide films.
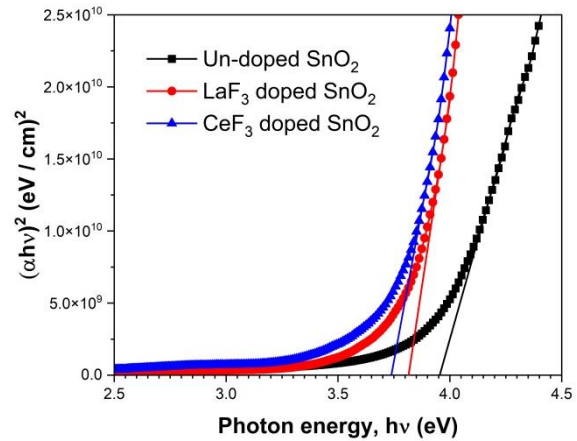
Figure 4. Estimated optical band gap (E_g) derived from the Tauc relation for tin oxide films doped with rare-earth fluoride.

Figure 3 illustrates the optical transmittance spectra of the examined films. The transmittance curves were recorded at ambient temperature over the wavelength range of 190-1100 nm. The average optical transmittance of all the deposited films was computed within the spectral range of 400 - 700 nm and is presented in Table 1. The un-doped SnO_2 exhibited an average transmittance of 87.1 %, which decreased to 84.3 % and 82.0 % for the LTFO and CTFO, respectively. Typically, the average transmittance of thin films depends on factors such as film thickness, grain size, surface roughness, and crystal imperfections. In this study, the decrease in transmittance observed in RF_3-doped SnO_2 films compared to the un-doped SnO_2 films may be attributed to the increased grain size and film thickness. The RF_3-doped SnO_2 films

exhibited larger grain sizes, resulting in rougher surfaces, which in turn led to increased scattering of photons [23]. Additionally, the rise in film thickness of the RF_3-doped SnO_2 films results in increased light absorption [24], consequently resulting in lower optical transmittance.

The plot of $(\alpha h\gamma)^2$ with respect to photon energy $(h\nu)$ for both un-doped SnO_2 and RFTO films is presented in Figure 4. The determination of the optical band gap (E_g) for a direct band gap semiconductor involves applying Tauc's equation [25]. The E_g values for the un-doped SnO_2 and RFTO films were calculated by extending the linear portion of the plots to the point where $(\alpha h\nu)^2$ equals zero on the energy axis. Table 1 lists the E_g values for all films. The optical band gap for un-doped SnO_2 film is 3.95 eV, showing a minor decrease to 3.81 eV and 3.74 eV with the addition of 2 mol.% LaF_3 and CeF_3 into SnO_2film, respectively. The determined optical band gap of our un-doped SnO_2 film, at 3.95 eV, aligns with the results reported in earlier studies, which range between 3.6 and 4.0 eV [26, 27]. The noted shift towards longer wavelengths in the optical band gap of the RFTO films can be explained by taking into account the *sp–f* exchange interactions that occur between the band electrons of the host material and the localized *f* electrons of the rare-earth doped ions. These ions replace Sn^{4+} in the lattice [28]. This phenomenon is ascribed to the compensatory influence of the holes produced by the dopant ions within the inherent n-type carriers [29].

3.3. Electrical properties

The Hall effect and Seebeck coefficient measurements results for the un-doped SnO_2 and RFTO films produced with a 2 mol.% concentration of RF_3 are displayed in Table 2.

Table 2. Electrical properties of un-doped and 2 mol% RF_3-doped SnO_2 thin films post-annealed at 475 ^{o}C.

Film	Resistivity, Ω cm	Carrier Conc. cm^{-3}	Hall mobility, cm^{2}V^{-1}s^{-1}	Seebeck Coeff. μVK^{-1}	Type of elec. conductivity
SnO_2	2.37×10^{-2}	-9.34×10^{18}	28.20	-171	n
LFTO	8.68×10^{-3}	$+8.82 \times 10^{19}$	8.15	$+132$	p
CFTO	1.70×10^{-2}	$+5.25 \times 10^{19}$	6.99	$+167$	p

The film conductivity type was determined using the Hall effect at ambient temperature, revealing the well-known n-type conductivity of the un-doped SnO_2 film. Conversely, the studied RFTO films exhibited p-type conductivity. Figure 5 illustrates the variation in electrical resistivity, hole concentration, and Hall mobility for both un-doped SnO_2 and RFTO films. The RFTO films exhibit decreased electrical resistivity and Hall mobility, along with an increased hole concentration compared to the un-doped SnO_2 film. The electrical resistivity of the un-doped SnO_2 film is 2.37×10^{-2} Ωcm, which reduces to 1.70×10^{-2} Ωcm and 8.68×10^{-3} Ωcm for the CFTO and LFTO films, respectively. The observed decrease and variation in the electrical resistivity of the RFTO films in this study can be attributed to the increase and alteration in carrier concentration [30, 31]. The un-doped SnO_2 film has a carrier concentration of 9.34×10^{18} cm^{-3}, whereas the 2 mol.% RF_3-doped SnO_2 films exhibit a significantly higher carrier concentration. The carrier concentration values for CFTO and LFTO are 5.25×10^{19} cm^{-3} and 8.82×10^{19} cm^{-3}, respectively, contributing to the reduction in electrical resistivity of CFTO-LFTO thin films. As per the information in Table 2, the Hall mobility for the un-doped SnO_2 film stands at 28.20 cm^{2}V^{-1}s^{-1}. The addition of 2 mol.% RF_3 to the SnO_2 film results in a sharp decline in Hall mobility, with values of 7.57 cm^{2}V^{-1}s^{-1} and 6.99 cm^{2}V^{-1}s^{-1} for LFTO and CFTO, respectively.

To further confirm the conduction type, additional Seebeck measurements were conducted over a temperature range of 300 to 345 K. As presented in Table 2, the un-doped SnO_2 thin film, with a Seebeck coefficient of -171 μV/K, indicating the presence of n-type conductivity. Upon doping the SnO_2 film with 2 mol.% RF_3, all RFTO films exhibited positive values of the Seebeck coefficient, measuring 167 μV/K and 132 μV/K for the CFTO and LFTO films, respectively, confirming their p-type conductivity. Table 2 additionally shows that the Seebeck coefficients follow the order of CFTO and LFTO, inversely proportional to hole concentrations. This trend aligns with the relationship between carrier concentration (n) and Seebeck coefficient (S), as described by the equation [32 - 34]:

$$S = \frac{8\pi^2 k_B^2}{3eh^2} m^* T \left(\frac{\pi}{3n} \right)^{2/3} \tag{1}$$

where m^* is the effective mass of the carrier. In short, the outcomes not only suggest that our investigated RFTO films are degenerate semiconductors but also align well with the Hall effect measurements.
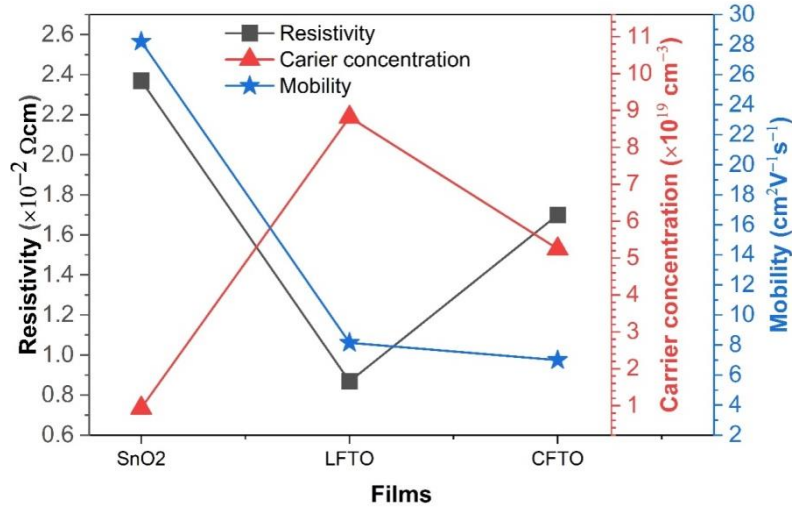
Figure 5. Electrical resistivity, carrier concentration, and Hall mobility of rare-earth fluoride-doped tin oxide films.

A potential explanation for the increase in hole concentration in RF_3-doped SnO_2 films could be attributed to the substitution of R^{3+} into Sn^{4+} sites and F^- into O^{2-} sites, thereby generating acceptor levels in the lattice. The plausible mechanism of p-type tin oxide resulting from RF_3 doping can be elucidated through the Kröger-Vink notation [35]. Accordingly, the Schottky defects in the fabricated SnO_2 can be articulated as follows:

$$O_O^X \rightarrow V_O^{\bullet\bullet} + 2e' \tag{2}$$

The equilibrium concentration of vacancies, denoted as nv, can be estimated as:

$$\frac{nv}{N} = exp\left(\frac{\Delta H}{2kT} \right) \tag{3}$$

where ΔH is the enthalpy of forming oxygen vacancy, N is the number of oxygen sites in the volume of concern, k is the Boltzmann constant, and T is 475 °C (748 K), upon which vacancy concentration is assumed to be quenched in after cooling down to ambient temperature. Taking the density of SnO_2 as 6.95 g/cm³, the mole-part of SnO_2 in one cm³ volume of the film is calculated as 0.04612 mole. The number of oxygen sites in a perfect SnO_2 crystal is $0.04612 \times 2 \times 6.02 \times 10^{23} = 5.55 \times 10^{22}$ cm⁻³. Taking the carrier concentration as 9.34×10^{18} cm⁻³ of the un-doped SnO_2 film, the fraction of oxygen becomes vacant, remembering that one oxygen vacancy creates two holes as in Eq. (2), $9.34 \times 10^{18}/(2 \times 5.55 \times 10^{22}) = 8.49 \times 10^{-5}$. This means that only 0.00849 % of oxygen sites that become vacant will dominate the conductivity of the un-doped SnO_2 film.

The enthalpy of the formation of an oxygen vacancy calculated according to Eq. (3) is 1.9×10^{-19} J or 1.19 eV. The value is small as compared with 5.99 eV, 3.61 eV, 9.75 eV, 6.58 eV, and 6.23 eV for the solid of SnO_2, ZnO, In_2O_3, CaO, and MgO, respectively. Now, assuming added RF_3 has dissolved into the SnO_2 lattice, based on the fact that no new phases exist in the XRD patterns. All possible defect reactions that involve Sn^{+4} lattice sites, O^{2-} lattice sites, oxygen vacancies, interstitial sites, and the dopant RF_3 are as follows:

1) One Sn^{4+} lattice site underwent substitution with one R^{3+} ion:

$$R_R^X \xrightarrow{SnO_2} R'_{Sn} + h^\bullet \tag{4}$$

2) Three vacant oxygen sites were substituted with three F^- ions:

$$3F_F^X + 3V_O^{\bullet\bullet} \rightarrow 3F_O^\bullet + 3h^\bullet \tag{5}$$

3) Two oxygen lattice sites underwent substitution with two F^- ions:

$$2F_F^X \rightarrow 2F_O^\bullet + 2e' \tag{6}$$

4) One F^- ion is introduced into one interstitial site:

$$F_F^X \rightarrow F_i' + h^\bullet \tag{7}$$

5) A R^{+3} ion that occupies an interstitial site:

$$R_R^X \rightarrow R_i^{\bullet\bullet\bullet} + 3e' \tag{8}$$

In theory, the five defect reactions prevail for all RF_3 doping concentrations. However, F^- has the strongest electro-negativity of all anions. As RF_3 dissolves F^- tends to fill the oxygen vacancies first due to the strong binding force F^- extends to surrounding cations. Furthermore, the ionic radii of the ions are $F^- = 1.19$ Å, $O^{2-} = 1.26$ Å, $Sn^{4+} = 0.83$ Å, $La^{3+} = 1.172$ Å, and $Ce^{3+} = 1.15$ Å, that each case of doping adds to the complexity. For instance, Eq. (5) is less likely to happen due to the limited availability of vacancies for replacement. Besides, Eq. (8) indicates that once an R^{+3} ion occupies an interstitial site, 3 electrons will be released. However, we can safely say that this reaction does not likely occur or leases a very small fraction of interstitial R^{3+} will endow an n-type conduction. We propose that main mechanisms dominating RF_3 added films are in equations (4), (6) and (7) in different competing potentials, based on the resultant p-type conduction of experimental facts.

Furthermore, the reduction in hole mobility observed in the RFTO films can be explained by equation (4), which corresponds to the heightened lattice distortion due to the larger R^{3+} ion replacing the smaller Sn^{4+} ion site, and equation (2), which relates to ionized impurity scattering centers induced by the interstitial F^- ions in the Sn^{4+}-O^{2-} lattice.

3.4. Optoelectronic properties of the transparent conducting oxide thin films

A transparent electrode films for optoelectronic application must possess favorable electrical and optical properties. The figure-of-merit (FOM) serves as a key benchmark for assessing the performance of transparent electrode materials, calculated using the Haacke formula [6].

$$FOM = \frac{T^{10}}{R_S} \tag{9}$$

Table 3. Comparing the electrical characteristics, average optical transmittance (T_{op}), and FOM between 2 mol.% RF_3-doped SnO_2 thin films and the earlier reported p-type and typical n-type TCO films.

Film	Resistivity (Ωcm)	Carrier Conc. (cm^{-3})	Hall mobility ($cm^2V^{-1}s^{-1}$)	T_{op} (%)	FOM (Ω^{-1})	Ref.
p-type LFTO	8.68×10^{-3}	8.82×10^{19}	8.15	84.3	6.59×10^{-4}	This study
p-type CFTO	1.70×10^{-2}	5.25×10^{19}	6.99	82.0	1.74×10^{-4}	This study
p-type $CuAlO_2$	1.05×10^{1}	1.30×10^{17}	10.4	~65	6.41×10^{-8}	[9]
p-type $CuGaO_2$	1.59×10^{1}	1.70×10^{18}	0.23	80	3.38×10^{-7}	[10]
p-type $CuBO_2$	0.61×10^{1}	10^{17}	~100	85	6.45×10^{-7}	[11]
p-type $CuCrO_2$	-	-	-	53.6	-	[13]
p-type $AgGaO_2$	3.13×10^{3}	-	-	> 50	-	[12]
p-type $FeSnO_2$	6.30×10^{1}	1.20×10^{16}	-	~90	1.94×10^{-7}	[14]
p-type $InGaO_3(ZnO)_5$	~10^5	~10^{13}	~80	> 80	-	[17]
p-type Cu:ZnCoO	3.26×10^{1}	4.40×10^{17}	2.69	-	-	[15]
p-type $AZO:Cu_2O$	6.90×10^{-3}	1.99×10^{20}	8.36	> 90	2.02×10^{-3}	[8]
p-type LaCuOS	0.34×10^{1}	7.15×10^{18}	0.26	> 50	2.32×10^{-8}	[18]
p-type $(La_{1-x}Sr_xO)CuS$	5.00×10^{-2}	-	-	> 60	1.81×10^{-6}	[19]
p-type NdCuOS:Ca5%	1.92×10^{-2}	9.00×10^{20}	0.36	54.3	4.70×10^{-6}	[3]
n-type ITO	5.88×10^{-4}	1.29×10^{20}	15.4	87	1.72×10^{-2}	[36]
n-type HFZO	7.50×10^{-4}	2.00×10^{20}	43	83	1.50×10^{-2}	[4]

where T is the transmittance at a wavelength of 550 nm, derived from the transmittance spectral data, while R_S is sheet resistance of the thin film, calculated using the van der Pauw technique based on the four-probe measurement results [37]. The FOM values for the RFTO films are detailed in Table 3. This also offers a recap and comparison of the optical transmittance, electrical properties, and the FOM of the p-type RFTO films in this study with those of p-type TCO films and conventional n-type indium tin oxide (ITO) and fluorinated and hydrogenated zinc oxide (HFZO) films from previous reports. From Table 3, it is evident that the FOM values for LFTO and CFTO are 6.59×10^{-4} Ω^{-1} and 1.74×10^{-4} Ω^{-1}, respectively. Compared to other p-type TCOs, these two RF_3-doped SnO_2 films exhibit exceptional performance. Notably, when compared to the best-performing $AZO:Cu_2O$ film (FOM = 2.02×10^{-3} Ω^{-1}), the FOM of the LFTO and CFTO films falls in the second range. Moreover, these p-type RFTO films are well-suited for integration with other n-type transparent conducting materials based on SnO_2 to create homojunctions, making them highly applicable for various p-n junction devices.

4. CONCLUSIONS

In this research, we present transparent conducting oxide thin films featuring p-type characteristics, with a thickness ranging from 246 to 287 nm. These films are derived from rare-

earth trifluoride-doped SnO_2, employing LaF_3 and CeF_3 as dopants. The films were fabricated using the sol-gel dip-coating method and subsequently subjected to post-annealing in air at 475 ^{o}C. The electrical conduction of the films underwent a transition from n-type in the case of un-doped SnO_2 to p-type for LaF_3- and CeF_3-doped SnO_2 films. This transition was verified through measurements of both Seebeck coefficient and Hall effect. P-type LaF_3- and CeF_3-doped SnO_2 films exhibit high transparency, with values of 84.3 % and 82.0 %, respectively, within the wavelength range of 400 - 700 nm. The optical band gap energy for these films falls between 3.74 eV and 3.81 eV, respectively. The electrical resistivity, carrier concentration, and Hall mobility of the RFTO films are in the range of $1.70 \times 10^{-2} – 8.68 \times 10^{-3}$ Ωcm, $5.25 \times 10^{19} – 8.82 \times 10^{19}$ cm^{-3}, and $6.99 – 8.15$ cm^{2}V^{-1}s^{-1}, respectively. These findings indicate that the p-type RFTO films are great potential for transparent electrodes in optoelectronic devices. They can seamlessly combine with transparent conducting films based on n-type SnO_2 to create homojunctions, making them highly applicable for various photonic devices incorporating p-n junctions.

CRediT authorship contribution statement. Van-Da Dao: Data processing, Writing manuscript. Quang-Phu Tran: Data processing, Manuscript editing, Supervision. Van-Hoi Pham: Methodology, Data analysis, Supervision.

Declaration of competing interest. The authors declare that they have no known competing financial interests or personal relationships that could have appeared to influence the work reported in this paper.

REFERENCES

1. He L., Luan C., Feng X., Xiao H., Yang X., Wang D., and Ma J. - UV–vis transparent conducting Ta-doped SnO_2 epitaxial films grown by metal-organic chemical vapor deposition, Materials Research Bulletin **118** (2019) 110488. https://doi.org/10.1016/j.materresbull.2019.05.013.

2. Feng M., Zhou H., Guo W., Zhang D., Ye L., Li W., Ma J., Wang G., and Chen S. - Fabrication of P-type transparent conducting CuxZn$_{1-x}$S films on glass substrates with high conductivity and optical transparency, Journal of Alloys and Compounds **750** (2018) 750-756. https://doi.org/10.1016/j.jallcom.2018.03.402.

3. Zhang N., Liu X., Shi D., Tang B., Annadi A., and Gong H. - Achievement of highly conductive p-type transparent NdCuOS film with Cu deficiency and effective doping, Materials Today Chemistry **10** (2018) 79-89. https://doi.org/10.1016/j.mtchem.2018.07.006.

4. Pham A. T. T., Nguyen P. T., Phan T. B., and Tran V. C. - Study on fluorination and hydrogenation in transparent conducting zinc oxide thin films, Vietnam Journal of Science and Technology **58** (2020) 197-203. https://doi.org/10.15625/2525-2518/58/2/14083.

5. Quynh T. D., Anh L. T. L., and Xuan N. S. - On the contribution factors of enhanced photocatalytic activity of doped semiconductors: Structural and optical investigation of Cu_{2+} doped ZnO nanoparticles, Vietnam Journal of Science and Technology **59** (2021) 277-289. https://doi.org/10.15625/2525-2518/59/3/15490.

6. Haacke G. - New figure of merit for transparent conductors, Journal of Applied Physics, **47** (1976) 4086-4089. https://doi.org/10.1063/1.323240.

7. Rozati S. M. and Ziabari S. A. M. - A review of various single layer, bilayer, and multilayer TCO materials and their applications, Materials Chemistry and Physics **292** (2022) 126789. https://doi.org/10.1016/j.matchemphys.2022.126789.

8. Hui K., Hui K. S., Li L., Cho Y., and Singh J. - Low resistivity p-type $Zn_{1-x}Al_xO:Cu_2O$ composite transparent conducting oxide thin film fabricated by sol–gel method, Materials Research Bulletin **48** (2013) 96-100. https://doi.org/10.1016/j.materresbull.2012.10.013.

9. Kawazoe H., Yasukawa M., Hyodo H., Kurita M., Yanagi H., and Hosono H. - P-type electrical conduction in transparent thin films of $CuAlO_2$, Nature **389** (1997) 939-942. https://doi.org/10.1038/40087.

10. Ueda K., Hase T., Yanagi H., Kawazoe H., Hosono H., Ohta H., Orita M., and Hirano M. - Epitaxial growth of transparent p-type conducting $CuGaO_2$ thin films on sapphire (001) substrates by pulsed laser deposition, Journal of Applied Physics **89** (2001) 1790-1793. https://doi.org/10.1063/1.1337587.

11. Snure M. and Tiwari A. - $CuBO_2$: A p-type transparent oxide, Applied Physics Letters **91** (2007) 092123. https://doi.org/10.1063/1.2778755.

12. Vanaja K., Ajimsha R., Asha A., and Jayaraj M. - p-type electrical conduction in α-$AgGaO_2$ delafossite thin films, Applied Physics Letters **88** (2006) 212103. https://doi.org/10.1063/1.2204757.

13. Xiong D., Xu Z., Zeng X., Zhang W., Chen W., Xu X., Wang M., and Cheng Y. B. - Hydrothermal synthesis of ultrasmall $CuCrO_2$ nanocrystal alternatives to NiO nanoparticles in efficient p-type dye-sensitized solar cells, Journal of Materials Chemistry **22** (2012) 24760-24768. https://doi.org/10.1039/C2JM35101C.

14. Bagheri-Mohagheghi M. M., Shahtahmasebi N., Alinejad M. R., Youssefi A., and Shokooh-Saremi M. - Fe-doped SnO_2 transparent semi-conducting thin films deposited by spray pyrolysis technique: Thermoelectric and p-type conductivity properties, Solid State Sciences **11** (2009) 233-239. https://doi.org/10.1016/j.solidstatesciences.2008.05.005.

15. Cao P., Zhao D., Shen D., Zhang J., Zhang Z., and Bai Y. - Cu^+-codoping inducing the room-temperature magnetism and p-type conductivity of ZnCoO diluted magnetic semiconductor, Applied Surface Science **255** (2009) 3639-3641. https://doi.org/ 10.1016/j.apsusc.2008.10.011.

16. Al-Jawhari H. A. - A review of recent advances in transparent p-type Cu_2O-based thin film transistors, Materials Science in Semiconductor Processing **40** (2015) 241-252. https://doi.org/10.1016/j.mssp.2015.06.063.

17. Nomura K., Ohta H., Ueda K., Kamiya T., Hirano M., and Hosono H. - Thin-film transistor fabricated in single-crystalline transparent oxide semiconductor, Science **300** (2003) 1269-1272. https://doi.org/10.1126/science.1083212.

18. Zhang N., Shi D., Liu X., Annadi A., Tang B., Huang T. J., and Gong H. - High performance p-type transparent LaCuOS thin film fabricated through a hydrogen-free method, Applied Materials Today **13** (2018) 15-23. https://doi.org/10.1016/ j.apmt.2018.08.003.

19. Hiramatsu H., Ueda K., Ohta H., Orita M., Hirano M., and Hosono H. - Preparation of transparent p-type ($La_{1-x}Sr_xO$)CuS thin films by rf sputtering technique, Thin Solid Films **411** (2002) 125-128. https://doi.org/10.1016/S0040-6090(02)00200-6.

20. Banerjee A. and Chattopadhyay K. - Recent developments in the emerging field of crystalline p-type transparent conducting oxide thin films, Progress in Crystal Growth and Characterization of Materials **50** (2005) 52-105. https://doi.org/10.1016/j.pcrysgrow.2005.10.001.

21. Kumari A., Panda R., Jha M. K., Kumar J. R., and Lee J. Y. - Process development to recover rare earth metals from monazite mineral: A review, Minerals Engineering **79** (2015) 102-115. https://doi.org/10.1016/j.mineng.2015.05.003.

22. Lizin A. A., Tomilin S. V., Gnevashov O. E., Gazizov R. K., Osipenko A. G., Kormilitsyn M. V., Baranov A. A., Zaharova L. V., Naumov V. S., and Ponomarev L. I. - PuF_3, AmF_3, CeF_3, and NdF_3 solubility in LiF–NaF–KF melt, Atomic energy **115** (2013) 11-17. https://doi.org/10.1007/s10512-013-9740-9.

23. Tran Q. P., Fang J. S., and Chin T. S. - Optical properties and boron doping-induced conduction-type change in SnO_2 thin films, Journal of Electronic Materials **45** (2016) 349-356. https://doi.org/10.1007/s11664-015-4081-1.

24. Bu I. Y. - Sol–gel deposition of fluorine-doped tin oxide glasses for dye sensitized solar cells, Ceramics International **40** (2014) 417-422. https://doi.org/10.1016/j.ceramint.2013.06.017.

25. Tran Q. P., Fang J. S., and Chin T. S. - Properties of fluorine-doped SnO_2 thin films by a green sol–gel method, Materials Science in Semiconductor Processing **40** (2015) 664-669. http://dx.doi.org/10.1016/j.mssp.2015.07.047.

26. Shanthi S., Subramanian C., and Ramasamy P. - Growth and characterization of antimony doped tin oxide thin films, Journal of Crystal Growth **197** (1999) 858-864. https://doi.org/10.1016/S0022-0248(98)01066-5.

27. Arefi-Khonsari F., Bauduin N., Donsanti F., and Amouroux J. - Deposition of transparent conductive tin oxide thin films doped with fluorine by PACVD, Thin Solid Films **427** (2003) 208-214. https://doi.org/10.1016/S0040-6090(02)01211-7.

28. Mazloom J. and Ghodsi F. - Spectroscopic, microscopic, and electrical characterization of nanostructured SnO_2:Co thin films prepared by sol–gel spin coating technique, Materials Research Bulletin **48** (2013) 1468-1476. https://doi.org/10.1016/j.materresbull.2012.12.069.

29. Ravichandran K. and Thirumurugan K. - Type inversion and certain physical properties of spray pyrolysed SnO_2:Al films for novel transparent electronics applications, Journal of Materials Science & Technology **30** (2014) 97-102. https://doi.org/10.1016/j.jmst.2013.09.019.

30. Saha B., Das S., and Chattopadhyay K. - Electrical and optical properties of Al doped cadmium oxide thin films deposited by radio frequency magnetron sputtering, Solar Energy Materials and Solar Cells **91** (2007) 1692-1697. https://doi.org/10.1016/j.solmat.2007.05.025.

31. Sakthivel P., Asaithambi S., Karuppaiah M., Sheikfareed S., Yuvakkumar R., and Ravi G. - Different rare earth (Sm, La, Nd) doped magnetron sputtered CdO thin films for optoelectronic applications, Journal of Materials Science: Materials in Electronics **30** (2019) 9999-10012. https://doi.org/10.1007/s10854-019-01342-9.

32. Heremans J. P., Jovovic V., Toberer E. S., Saramat A., Kurosaki K., Charoenphakdee A., Yamanaka S., and Snyder G. J. - Enhancement of thermoelectric efficiency in PbTe by distortion of the electronic density of states, Science **321** (2008) 554-557. https://doi.org/10.1126/science.1159725.

33. Snyder G. J. and Toberer E. S. - Complex thermoelectric materials, Nature Materials **7** (2008) 105-114. https://doi.org/10.1038/nmat2090.

34. Dusastre V. - Materials for sustainable energy: a collection of peer-reviewed research and review articles from Nature Publishing Group, World Scientific, London, 2011.

35. Kröger F. A. - The Chemistry of Imperfect Crystals: Imperfection Chemistry of Crystalline Solids, North-Holland, Holland, 1974.

36. Ruan C., Sun Q., Xiao D., Li H., Xia G., and Wang S. - Lightwave irradiation-assisted low-temperature solution synthesis of indium-tin-oxide transparent conductive films, Ceramics International **48** (2022) 12317-12323. https://doi.org/10.1016/j.ceramint.2022.01.094.

37. Kim J., Yun H., Seo J., Kim J. H., Kim J. H., Mkhoyan K. A., Kim B., and Char K. - Deep-UV Transparent Conducting Oxide La-Doped $SrSnO_3$ with a High Figure of Merit, ACS Applied Electronic Materials **4** (2022) 3623-3631. https://doi.org/10.1021/acsaelm.2c00581.